

Convective craton self-compression and its role for stabilization of old lithosphere

¹Jyotirmoy Paul

²Clinton P. Conrad

^{3,4,5}Thorsten W. Becker

⁶Attrjee Ghosh

¹Bayerisches GeoInstitut, Universität Bayreuth

²Centre for Earth Evolution and Dynamics (CEED), Department of Geosciences, University of Oslo

³Institute for Geophysics, Jackson School of Geosciences, The University of Texas at Austin

⁴Department of Geological Sciences, Jackson School of Geosciences, The University of Texas at Austin

⁵Oden Institute for Computational Engineering & Sciences, The University of Texas at Austin

⁶Centre for Earth Sciences, Indian Institute of Science, Bangalore

Key Points:

- Cratons self-induce inwardly convergent tractions along their periphery, giving rise to regional compressive regimes within them.
- Compression arises due to the diversion of mantle flow in the presence of thick and viscous cratons.
- Convective self-compression could help in stabilizing older lithosphere against mantle shearing.

20 **Abstract**

21 Despite being exposed to convective stresses for long times, cratonic roots appear capable
 22 of resisting mantle shearing. This tectonic stability can be attributed to their neutral
 23 density and higher strength, i.e., viscosity. But such high viscosity also leads to higher
 24 tractions along their edges compared to other parts of the lithosphere. We develop instantan-
 25 eous global spherical numerical models incorporating present-day thick cratons
 26 embedded in a convecting mantle to further investigate the origin of these high trac-
 27 tions surrounding cratons. Our results show that mantle flow can be diverted downward due
 28 to thick and viscous cratonic roots, giving rise to elevated inwardly convergent trac-
 29 tions along the craton periphery. The velocity diversion associated with the change in trac-
 30 tions can also induce regional compressive stress regimes within cratons. Such compres-
 31 sion could serve to stabilize older continental lithosphere against mantle shearing, adding
 32 an additional factor in cratons' longevity.

33 **Plain Language Summary**

34 Cratons are the oldest continental relicts on Earth. Due to Earth's plate tecton-
 35 ics and mantle convection, many non-cratonic rocks get recycled. However, cratons have
 36 escaped the tectonic recycling, and some remained stable for more than ~ 3 billion years.
 37 Previous studies have shown that cratons' high strength and neutral buoyancy provide
 38 them with tectonic stability. This study shows that cratons can self-induce compression
 39 along their edges due to the thick and highly viscous roots. Such compressive stresses
 40 may further help to stabilize the older lithosphere.

41 **1 Introduction**

42 Cratons are relics of the oldest continental lithosphere, surviving since the Archean
 43 (Pearson & Wittig, 2014; Pearson et al., 1995; Pearson, 1999). Structurally, cratons have
 44 thick lithospheric roots, or cratonic keels (Gung et al., 2003; Polet & Anderson, 1995),
 45 that are likely cold because they are characterized by fast seismic velocities (Auer et al.,
 46 2014; Ritsema et al., 2011; Simmons et al., 2010). Low measured heat fluxes of cratonic
 47 lithosphere reaffirm the argument for colder cratons (Rudnick et al., 1998). The endurance
 48 of Archean cratons against Earth's tectonic and convective recycling is highly debated
 49 (cf. Yoshida & Yoshizawa, 2021), but proposed reasons for cratonic stability draw from
 50 geochemical and geophysical perspectives (Jordan, 1975, 1978; King, 2005; Lenardic &
 51 Moresi, 1999; Lenardic et al., 2003; Paul et al., 2019; Paul & Ghosh, 2020; Sleep, 2003;
 52 O'Neill et al., 2008; Wang et al., 2014; Yoshida, 2012). One of the oldest hypotheses pro-
 53 posed that cratons are constituted of chemically lighter elements that help them to float
 54 above the convective mantle without sinking into it (Jordan, 1975, 1978). However, sub-
 55 sequent numerical models showed that chemical buoyancy alone cannot protect cratons
 56 from the continuous convective shearing exerted by the mantle flow. Instead, root thick-
 57 ness and viscosity are the two prime factors that can resist deformation against man-
 58 tle shearing (Lenardic & Moresi, 1999; Lenardic et al., 2003; O'Neill et al., 2008; Paul
 59 et al., 2019; Paul & Ghosh, 2020; Sleep, 2003).

60 To understand the role of craton viscosity, previous studies quantified the nature
 61 of tractions exerted by mantle flow at the base of the lithosphere, and the strain-rates
 62 associated with deformation there (Conrad & Lithgow-Bertelloni, 2006; Cooper & Con-
 63 rad, 2009; Naliboff et al., 2009; Paul et al., 2019). Conrad & Lithgow-Bertelloni (2006)
 64 showed that tractions increase as the lithospheric thickness increases. Paul et al. (2019)
 65 found a similar amplification of tractions, but also showed that the strain-rates at the
 66 cratonic base diminish as lithospheric roots get thicker. This inverse relation between
 67 tractions and the strain-rates may slow the deformation of a cratonic root, and there-
 68 fore might be an important factor for the long-term survival of cratons. Cooper & Con-
 69 rad (2009) attributed elevated tractions at the base of cratons to greater coupling to man-

tle flow, which has been noted in models with thick cratonic roots (Zhong, 2001; Becker, 2006). However, more recent models, especially those employing free-slip surface boundary conditions that more closely resemble Earth's own conditions, show that tractions are primarily amplified along the periphery of cratons (fig. 3 from Paul et al., 2019). Although Paul et al. (2019) speculated that cratonic edges might more effectively absorb mantle stresses compared to cratonic interiors, a proper quantitative analysis of such a phenomenon is lacking.

Here, we explore the origin of higher tractions along craton boundaries and consider their implications on the stability of cratons. We develop instantaneous spherical numerical models of mantle convection and examine how mantle flow is modified due to the presence of thick and viscous cratons. We hypothesize that cratons' high viscosity roots can divert mantle flow, which may induce elevated traction magnitude with an inwardly convergent direction at the craton periphery. We test our hypothesis using various models having different viscosities for cratons, asthenosphere and non-cratonic lithosphere. Finally, we consider how such high tractions generated by the cratons themselves may support cratonic stability against mantle shearing, and therefore could be essential to cratonic longevity.

2 Mantle convection models

We use the finite element code CitcomS to develop instantaneous spherical models of mantle convection (Zhong et al., 2000). The code assumes the mantle to be a viscous and incompressible fluid. It solves the conservation of mass, momentum, and energy equations with the Boussinesq approximation and infinite Prandtl number. The smallest resolution of our models in the horizontal direction is $\sim 0.7^\circ \times 0.7^\circ$. The vertical resolution in the top 300 km is 24 km, and from 300 km to CMB it is ~ 50 km. Mantle flow is driven by the density anomalies obtained from SMEAN2 seismic tomography (Jackson et al., 2017), which is a combination of S40RTS (Ritsema et al., 2011), GyPSuM-S (Simmons et al., 2010) and SAVANI (Auer et al., 2014) models. A velocity-density scaling value of 0.25 is used to convert velocity anomalies into density anomalies (cf. Paul et al., 2019). Higher velocity regions under the continents were removed till 300 km to impose neutrally buoyant cratons (cf. Paul et al., 2019). We keep a free-slip boundary condition at the surface and at the core-mantle boundary. Reference viscosity, Rayleigh number (Zhong et al., 2000), thermal expansivity and the thermal conductivity values are kept at $\eta_0 = 10^{21}$ Pa.s, $Ra = 4 \times 10^8$ (considering Earth radius as the length scale), $\alpha = 3 \times 10^{-5} \text{K}^{-1}$, and $\kappa = 10^{-6} \text{m}^2/\text{s}$ respectively.

In our models, the mantle is divided into four layers based on their relative viscosity w.r.t. to the upper mantle (300-600 km) reference viscosity, η_0 . The top 100 km is assigned as the lithosphere, which is $30\times$ more viscous than the reference mantle viscosity. Asthenosphere (100-300 km) is made 10x weaker than the reference mantle, having a relative viscosity of 0.1, and the lower mantle (660-2900 km) is made $50\times$ stronger than the reference mantle. On top of this radially-varying viscosity structure, we impose lateral viscosity variations. We approximate temperature-dependent viscosity using a linearised Arrhenius law $\eta = \eta_0 \times \exp(E(T_0 - T))$, where η_0 is the radial viscosity of any layer, T_0 is the non-dimensionalized reference temperature, and T is the non-dimensionalized actual temperature. In our models, the reference temperature T_0 is set to 0.5, and the range of non-dimensional temperature varies from 0 - 1, where the maximum temperature (1) corresponds to $\Delta T = 1300^\circ$ C. E is a dimensionless number that controls the strength of temperature dependence. We have tested several models to find the suitable values of E (cf. Paul et al., 2019) and keep it to 5. Temperature-dependent viscosity produces $10\times$ weak plate margins compared to the continental interiors. We also incorporate high viscosity cratons in our models, where the locations of cratons are taken from the 3SMAC model (Nataf & Ricard, 1996). Cratons are made $10\times$, $100\times$, and $1000\times$ more viscous than the surrounding lithosphere, and they have uniformly viscous keels

122 up to a depth of 300 km (Paul et al., 2019). We have also varied the relative viscosity
 123 of asthenosphere to 0.01 (10^{19} Pa.s) and 1 (10^{21} Pa.s) to test the consistency of our re-
 124 sults with respect to the radial viscosity structure of the mantle. In one of the cases, we
 125 have made lithosphere highly viscous with a relative viscosity 150 times the reference
 126 value. Our reference model omit cratons and only incorporates temperature-dependent
 127 viscosity to create lateral viscosity variations.

128 3 Traction within cratons

129 We analyse the $r\phi$ and $r\theta$ components of stress tensor ($\sigma_{ij}; i, j = r$: radial compo-
 130 nent, ϕ : longitudinal component, θ : co-latitudinal component) from model outputs
 131 and calculate traction vectors ($\vec{\tau}_0$) from the reference model (Fig. 1). In the reference
 132 model, the magnitudes of traction vectors are of order ~ 5 MPa, and their orientations
 133 are guided by density anomalies imposed in the model (Fig. 1 a). Incorporating $100\times$
 134 viscous cratons in the same model significantly affects traction vectors ($\vec{\tau}$) along the edge
 135 of cratons (Fig. 1b). A few zoomed-in maps near the cratonic regions show this effect
 136 more prominently (Figs. 1 c-i). Most cratons show rings of high traction magnitude around
 137 their periphery, where traction directions become inwardly convergent. Elevated inwardly
 138 convergent tractions appear prominently along the western margin of North and South
 139 American cratons (Figs. 1 c,d), north and south margin of the Scandinavian craton (Figs.
 140 1 f), east and south margin of Siberian and Australian craton (Figs. 1 e,g), east mar-
 141 gin of African cratons (Figs. 1 h). Indian craton being very small in size experiences con-
 142 vergent tractions all around it (Figs. 1 i). Southern most part of the African craton shows
 143 an outwardly directed traction, which is the only exception (Figs. 1 h).

144 To quantify the increment of traction magnitudes in the presence of cratons, we
 145 normalize the traction magnitude from models with craton to the reference model ($|\vec{\tau}|/|\vec{\tau}_0|$).
 146 In the presence of cratons that are $100\times$ more viscous than the rest of the lithosphere,
 147 the maximum traction ratio increases by up to $80\times$ to $100\times$ at ~ 120 km depth along
 148 the edge of cratons (Fig. 1 c-i). The magnitude of the traction ratio along the craton
 149 edges can be influenced by the viscosity structure imposed in our models (Fig. 2). To
 150 investigate the dependence of viscosity structure and depth on the traction ratio, we cal-
 151 culate the average traction ratio at various depths along the edges of cratons (Fig. 2 a).
 152 The edge of the cratons is identified by regions with more than 5 MPa. The general trend
 153 shows that the average traction ratio is close to 15 within the top 100 km of cratons, where
 154 they are surrounded by viscous lithosphere. The average traction ratios increase with
 155 depth, reaching peak values in the mid-craton depth range ~ 160 km. The highest trac-
 156 tion ratio at this depth could occur as the horizontal velocity reaches the peak velocity
 157 in the mid-asthenosphere depth. With increased depth, the traction ratio gradually falls
 158 before reaching another peak near the base of cratons at ~ 270 km depth. The exact mag-
 159 nitude of the traction ratio depends on the combination of the craton and asthenosphere
 160 viscosity. Highly viscous ($1000\times$) cratons exhibit the largest traction ratios, which reach
 161 their peak value between 30-35 in the mid-asthenospheric depth region. Models with smaller
 162 viscosity contrasts (e.g., stronger asthenosphere with relative viscosity 1) exhibit rela-
 163 tively smaller tractions at the craton edges, whereas weaker asthenosphere (relative vis-
 164 cosity 0.1, 0.01) is consistent with larger tractions. We have tested a model with high
 165 lithospheric viscosity ($150\times$) and similarly found large traction ratios along cratons' pe-
 166 riphery. In this case, the average traction ratio follows the same trend, except in the top
 167 100 km, where the average ratio becomes even larger up to 20 due to strong lithosphere.

168 We show the lithospheric stress state by plotting centroid moment tensor (CMT)
 169 type symbols to quantify the state of stress within cratons due to inwardly convergent
 170 tractions. CMT symbols are colored by the ratio of mean horizontal stress ($\sigma_h = 1/2(\sigma_{\phi\phi} + \sigma_{\theta\theta})$)
 171 and the second invariant of deviatoric stress ($\sigma_{II} = \sqrt{\sigma_{ij}\sigma_{ij}}$). A negative ratio indicates
 172 a compressive stress regime and vice-versa. CMT solutions imply that the model with-
 173 out craton has compression only along the convergent plate boundaries, i.e., along the

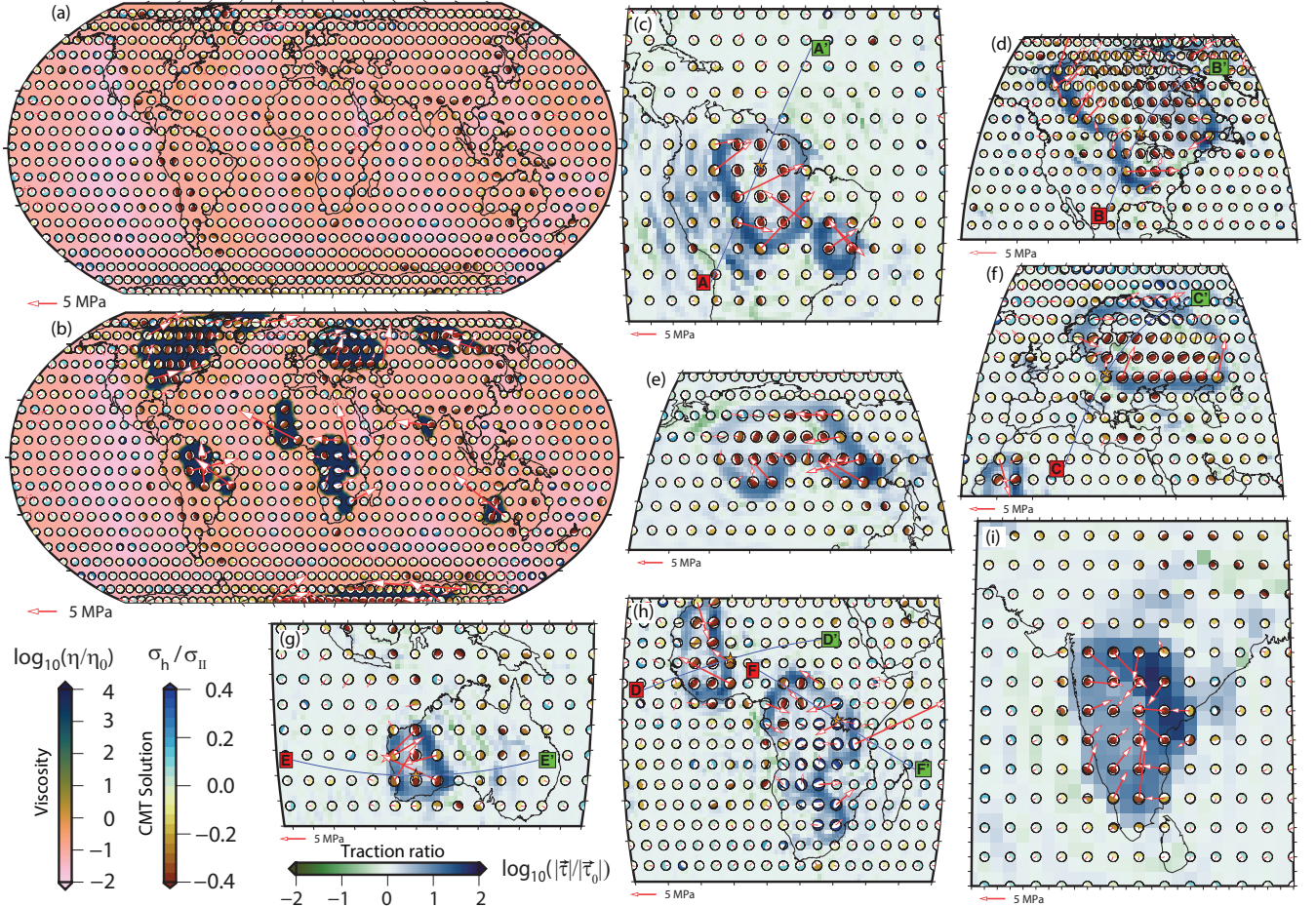


Figure 1. Global traction patterns and stress regimes in the absence and presence of cratons at 120 km depth. (a) Traction in reference model without cratons, (b) Traction in model with 0.1 relative viscosity of asthenosphere and cratons that are 100× more viscous than the surrounding lithosphere. Background colors indicate viscosity, and arrows represent the magnitude and direction of absolute traction. CMT symbols are colored as the ratio of mean stress to the second invariant of deviatoric stress (σ_h/σ_{II}), where negative values represent compressive stress regimes. (c)-(i) Zoomed-in plots near cratonic regions of South America (c), North America (d), Siberia (e), Scandinavia(f), Australia (g), Africa (h), and India (i). The background colors in (c-i) represent the logarithm of the traction ratio ($\log_{10}(|\vec{\tau}|/|\vec{\tau}_0|)$). Velocity cross-sections along the six transects (AA' - FF') are shown in Fig. 4

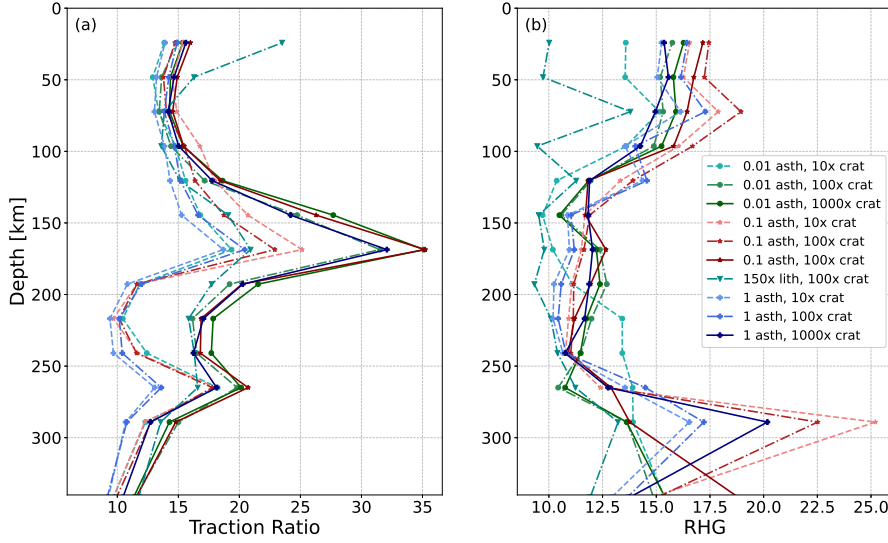


Figure 2. (a) Depth variation of the average traction ratio along the craton periphery from different models. (b) Depth variation of the ratio of horizontal velocity gradient (RHG) along the craton periphery from different models. A description of the different models is given in the index box. The first number in the box indicates the relative viscosity of the asthenosphere, and the second number indicates the viscosity multiple of cratons with respect to the lithosphere. (150× lith, 100× crat) represents a model with lithosphere relative viscosity of 150, and the asthenosphere relative viscosity is kept at 0.1.

margin of the Pacific, Indo-Eurasia collision zone. The same model with 100× viscous cratons can acquire a compressive stress regime within all cratons, except in South Africa. Apart from the South African craton, the state of compressive stress is omnipresent in all cratons regardless of their viscosity structure.

4 Origin of compression along craton periphery

Our models demonstrate a change of traction to a highly compressive state in the presence of viscous cratons. However, the origin of such a regional compressive regime in the presence of thick and viscous cratons needs to be investigated. The traction vector is calculated from $\sigma_{r\phi}$ and $\sigma_{r\theta}$, where

$$\sigma_{r\phi} = 2\eta \left(\frac{\partial v_\phi}{\partial r} + \frac{\partial v_r}{\partial \phi} \right) \quad (1)$$

$$\sigma_{r\theta} = 2\eta \left(\frac{\partial v_\theta}{\partial r} + \frac{\partial v_r}{\partial \theta} \right) \quad (2)$$

v_ϕ , v_θ , and v_r are the horizontal and vertical components of the velocity vector and η is the viscosity. The magnitude of traction is given by

$$|\vec{\tau}| = 2\eta \sqrt{\left(\frac{\partial v_\phi}{\partial r} + \frac{\partial v_r}{\partial \phi} \right)^2 + \left(\frac{\partial v_\theta}{\partial r} + \frac{\partial v_r}{\partial \theta} \right)^2} \quad (3)$$

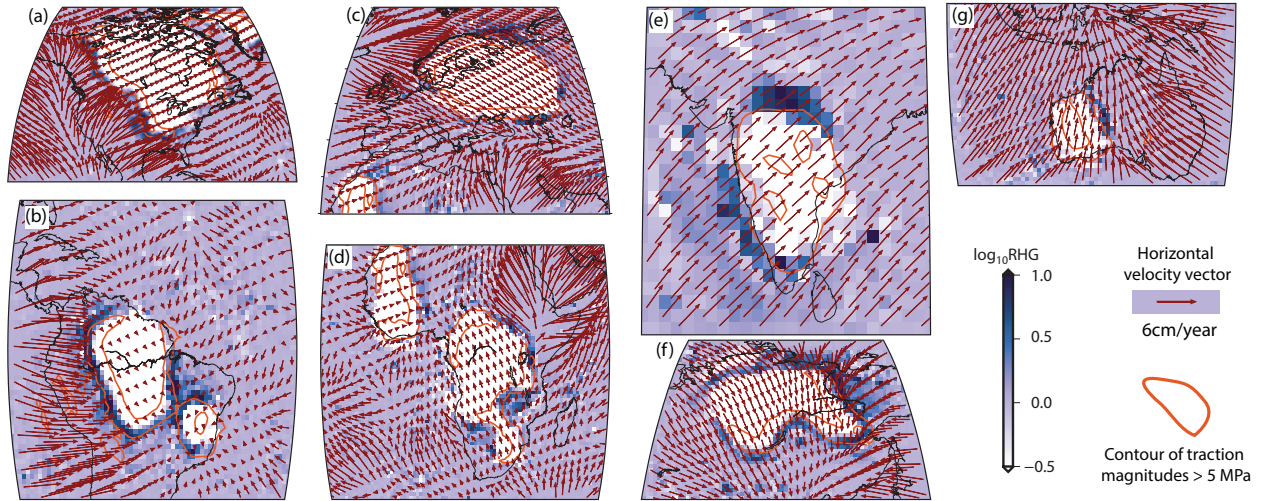


Figure 3. Zoomed-in maps of the ratio of horizontal velocity gradients of vertical velocity (RHG) at 120 km depth near different cratonic regions. Horizontal velocity vectors are plotted on top of it. Orange lines encircle areas where the traction magnitude is more than 5 MPa

186 Conceptually, the presence of a thick and highly viscous craton can obstruct asthenospheric flow in horizontal direction, and could deflect it downward. Such velocity diversion
 187 can make the v_θ and v_ϕ components extremely small near the craton edge, implying
 188 that the first terms in equations 1 and 2 will be negligible. With stronger downward
 189 diversion, the vertical velocity (v_r) component along the horizontal direction increases
 190 gradually towards cratons. Hence, the horizontal gradient of the vertical velocity com-
 191 ponents, i.e., the second term in the equation 1 and 2 become the controlling factor for
 192 the origin of high tractions along craton boundaries. We test this hypothesis by calcu-
 193 lating the horizontal gradient of vertical velocities as:

$$\nabla_h^v = \sqrt{\left(\frac{\partial v_r}{\partial \phi}\right)^2 + \left(\frac{\partial v_r}{\partial \theta}\right)^2} \quad (4)$$

195 To analyze the effect of thick cratons in changing the gradient, we take the ratio of the
 196 horizontal velocity gradient (RHG) as:

$$RHG = \frac{(\nabla_h^v)_{\text{craton}}}{(\nabla_h^v)_{\text{no_craton}}} \quad (5)$$

197 $(\nabla_h^v)_{\text{craton}}$ and $(\nabla_h^v)_{\text{no_craton}}$ are the horizontal gradient of vertical velocities from
 198 models with and without cratons, respectively. RHG can quantify the concentration of
 199 downward flow due to the presence of viscous cratons, where $RHG \gg 1$ indicates stronger
 200 vertical velocity deflection. Similar to the rings of high traction zones, we find rings of
 201 elevated RHG along the craton periphery (Fig. 3). Elevated RHG values can be inter-
 202 preted as horizontal velocities converting into vertical velocities near the craton bound-
 203 ary due to self-induced downwelling. The horizontal velocities are much reduced within
 204 cratons compared to their surroundings (Fig. 3). The amount of velocity reduction sig-
 205 nificantly depends on the craton size. Large cratons can resist mantle flow more efficiently
 206 compared to smaller cratons. Therefore, the horizontal velocity reduction within the North
 207 American, South American, Scandinavian, African, and Siberian craton are easily vis-
 208 ible (Fig. 3a-d,f). In contrast, the same is not pronounced within smaller cratons like
 209 India and Australia (Fig. 3e,g). Variation of velocity gradient is also controlled by the
 210 angle between the craton edge and horizontal flow. In our density-driven flow models,

the mantle flows from west to east under the North American plate, remaining almost perpendicular to the western face of the craton (Fig. 3a). Hence, maximum velocity diversion or highest RHG value occurs along the western margin of the North American craton. On the contrary, the south eastern margin of the craton, being almost parallel to flow, shows no significant change in RHG values. This pattern maps perfectly with the change of traction vector along the coast of the North American craton (Fig. 1d), where elevated tractions are observed along the western and the eastern margin of the North American craton, leaving out the southern and northern margins. Similar is observed for the western margin of the South American craton (Fig. 3b), north and South margin of the Scandinavian craton (Fig. 3c), east margin of African cratons (Fig. 3d), and east and south margin of Siberian (Fig. 3f) and Australian craton (Fig. 3g). Contours of traction magnitude > 5 MPa are plotted to visualize the coherence of high RHG value and zones of high traction on the craton edges. We investigate how this downwelling varies with the depth and viscosity structures in our models. We consider areas of high RHG values (≥ 5) that occur along the craton periphery and calculate their average (Fig. 2b). In the top 100 km, the average RHG varies within 15-17, except for the 150 viscous lithosphere case. In the mid-cratonic depth range (100-250 km), the average RHG value decreases slightly and varies within 10-13. Beyond 250 km depth, RHG increases again, reaching a peak near the base of cratons, likely because of the concentrated flow below them.

We compare the velocity cross-sections from our models with and without cratons to investigate the actual nature of flow velocity diversion along cratons. Cross-sections underneath the South American and the North American cratons show notable changes in velocity along their western margin. In both cases, the mantle flows from west to east without craton due to density differences imposed in our models (Figs. 4a-d). Convergent flow west of the South American craton occurs due to a subducting slab. In the presence of a thick and viscous craton, the convergent flow velocity is diverted along the craton margin and gets concentrated below it (Fig. 4 b). Similar velocity diversion is also visible around the western margin of the North American craton, where the flow gets diverted downwards and concentrated below the craton (Fig. 4 d). Flow diversion occurs along the north south direction of Scandinavian craton (Fig. 4 e,f). However, the diversion is relatively weaker most likely due to the absence of any slab pull force in the proximity. Weaker velocity diversion is also reflected in less elevated traction magnitude compared to the American cratons. The size of the Western African craton is significantly smaller than the rest, but the change of velocity field is considerably pronounced (Fig. 4 g, h). A downward flow along the Eastern margin of the craton denotes the change in RHG (Fig. 4 h). Australian craton also show a slight velocity diversion (Fig. 4 i,j) along an east west profile. Due to the smaller size of cratons (e.g., Indian craton), diversion of velocity vectors may not be visible clearly. Nevertheless, tractions result from velocity gradient multiplied with viscosity (see equation 3). Viscosity being a very large number (of the order of 10^{21}), a minimal change of velocity gradient can produce a sharp variation in the traction magnitude and direction. One significant change is observed for the South African craton where the mantle flows upward (Fig. 4f). In this scenario, the horizontal velocities get diminished due to the craton, and vertical velocities become stronger along the craton boundary. Therefore, the traction magnitude increases along the South African craton margin like the others, but the stress regime becomes extensional.

5 Implications for craton stabilization

The combined effect of viscosity and thickness of cratons causes them to self-compression within them. The traction magnitudes increase along the craton periphery, and their direction becomes inwardly convergent inside cratons. Magnitudes depend on the viscosity structure of the craton, asthenosphere, and lithosphere. In the presence of a $100 \times$ viscous craton, traction magnitude goes up to 15-20 MPa (Figs. 1b-i) which is almost

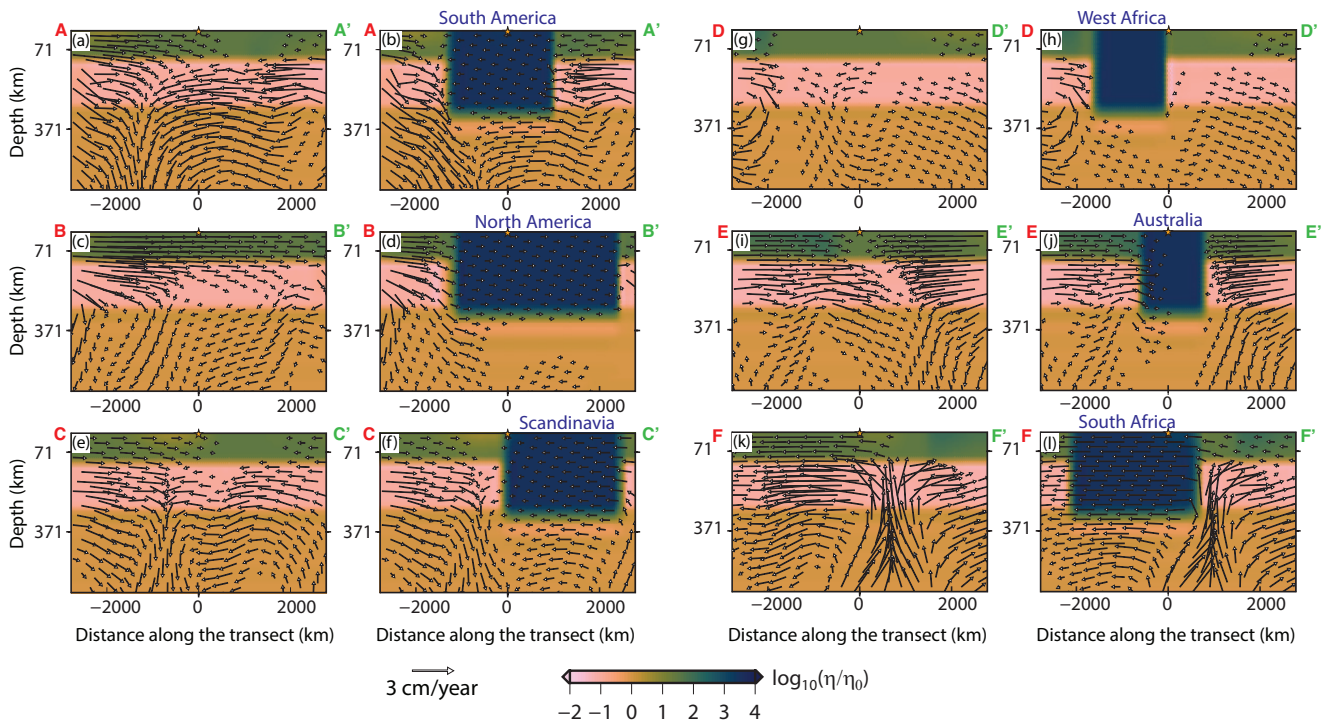


Figure 4. Comparison of velocity cross-sections without and with cratons along the transects shown in Fig. 1(c-i). Each figure is paired where the left figure shows the velocity profile without crater, and the right figure shows the same with crater. The name of the crater is given in all corresponding right-side figures. Background colors represent the logarithm of relative viscosity, and the arrows represent velocity vectors along the transect.

1-2 orders larger than the case without presence of cratons (Fig. 2a). The inward-directed orientation of tractions along the craton boundary appears to be a universal phenomenon (Figs. 1b), except the southern most part of the African craton. We infer that such convergent tractions originate from the diversion of mantle flow velocity due to the thick and viscous cratonic roots. We test our hypothesis by calculating the ratio of the horizontal gradient of vertical velocity (RHG, equation 5). Our calculations demonstrate that the mantle flow starts downwelling along craton margins, and this velocity gradient controls the state of traction along the craton periphery. Due to the downward diversion of mantle flow, it induces a compressive stress regime in all cratons.

Previous studies have attributed the long-term stability of cratons to their combined effect of thickness, viscosity, and chemical buoyancy (Lenardic et al., 2003; Paul et al., 2019). We suggest that self-induced compressive tractions along craton boundaries could be another critical factor that has made cratons stable across billions of years. Geologically cratons are not a single unit; instead, they are composed of multiple protocratons to form a larger continental mass (Bleeker, 2003). For example, the North American craton is composed of Superior, Slave, Wyoming, Hearne, Rae, and several other small blocks (Canil et al., 2008); the Indian craton is assembled with five smaller units, Dharwar, Bastar, Singhbhum, Bundelkhand, and Aravalli (Pandey, 2020). Since their formation and amalgamation, larger continental units have remained together for more than a couple of billion years. There are some instances of delamination or partial destruction of cratons (Liu et al., 2021; Menzies et al., 1993), but none of them were completely split apart. Self-compression could be a key reason the older continental units did not split away during the supercontinental break-up events.

A few recent studies found that partially destroyed cratons may re-achieve their original thickness within a few hundred million years. Numerical models have suggested a few mechanisms of such recratonization by plumes (Liu et al., 2021) or by a cycle of delamination and relamination (Peng et al., 2022). We infer, convective self-compression of cratons could also be a potential factor in such recratonization events. A compressive environment can slowly squeeze cratonic lithosphere to increase their thickness gradually over time. A temporary period of thin craton may exist when the destruction event is relatively recent and self-compression does not get enough time to heal the craton thickness. The destruction of the North China (Wu et al., 2019) and the Indian craton (Pandey, 2016; Paul & Ghosh, 2022) occurred during the Mesozoic, and they are currently thought to be partially thinned. However, the partially destroyed Slave craton during the Proterozoic is considered to have regained its original thickness (Liu et al., 2021). In the future, it will be interesting to develop time-dependent numerical models to study the effect of self-compression in the recratonization process.

300 **Acknowledgments**

301 All models were developed in Cray XC40 system at the Supercomputer Education and
 302 Research Centre (SERC), IISc. This work was supported by the Norwegian Research Coun-
 303 cil projects 223272 (Centre of Excellence) and 288449 (MAGPIE Project).

304 **References**

- 305 Auer, L., Boschi, L., Becker, T., Nissen-Meyer, T., & Giardini, D. (2014). Savani:
 306 A variable resolution whole-mantle model of anisotropic shear velocity varia-
 307 tions based on multiple data sets. *Journal of Geophysical Research: Solid Earth*,
 308 119(4), 3006–3034.
- 309 Becker, T. W. (2006). On the effect of temperature and strain-rate dependent vis-
 310 cosity on global mantle flow, net rotation, and plate-driving forces. *Geophysical*
 311 *Journal International*, 167(2), 943–957.
- 312 Bleeker, W. (2003). The late Archean record: a puzzle in ca. 35 pieces. *Lithos*, 71(2-
 313 4), 99–134.
- 314 Canil, D., et al. (2008). Canada's craton: a bottoms-up view. *GSA TODAY*, 18(6),
 315 4.
- 316 Conrad, C. P., & Lithgow-Bertelloni, C. (2006). Influence of continental roots and
 317 asthenosphere on plate-mantle coupling. *Geophysical Research Letters*, 33, L05
 318 312, doi:10.1029/2005GL025621.
- 319 Cooper, C., & Conrad, C. P. (2009). Does the mantle control the maximum thick-
 320 ness of cratons? *Lithosphere*, 1(2), 67–72.
- 321 Gung, Y., Panning, M., & Romanowicz, B. (2003). Global anisotropy and the thick-
 322 ness of continents. *Nature*, 422(6933), 707–711.
- 323 Jackson, M. G., Konter, J. G., & Becker, T. W. (2017). Primordial helium entrained
 324 by the hottest mantle plumes. *Nature*, 542, 340–343.
- 325 Jordan, T. (1975). The continental tectosphere. *Reviews of Geophysics*, 13(3), 1–
 326 12.
- 327 Jordan, T. (1978). Composition and development of the continental tectosphere. *Na-
 328 ture*, 274(5671), 544–548.
- 329 King, S. (2005). Archean cratons and mantle dynamics. *Earth and Planetary Sci-
 330 ence Letters*, 234(1), 1–14.
- 331 Lenardic, A., & Moresi, L. N. (1999). Some thoughts on the stability of cratonic
 332 lithosphere: effects of buoyancy and viscosity. *Journal of Geophysical Research:*
 333 *Solid Earth*, 104(B6), 12747–12758.
- 334 Lenardic, A., Moresi, L. N., & Mühlhaus, H. (2003). Longevity and stability of
 335 cratonic lithosphere: insights from numerical simulations of coupled mantle con-
 336 viction and continental tectonics. *Journal of Geophysical Research: Solid Earth*,
 337 108(B6), https://doi.org/10.1029/2002JB001859.
- 338 Liu, J., Pearson, D. G., Wang, L. H., Mather, K. A., Kjarsgaard, B. A., Schaeffer,
 339 A. J., ... Armstrong, J. P. (2021). Plume-driven recratonization of deep continen-
 340 tal lithospheric mantle. *Nature*, 592(7856), 732–736.
- 341 Menzies, M. A., Fan, W., & Zhang, M. (1993). Palaeozoic and Cenozoic lithoprobes
 342 and the loss of c. 120 km of Archean lithosphere, Sino-korean craton, China. *Geo-
 343 logical Society, London, Special Publications*, 76(1), 71–81.
- 344 Naliboff, J. B., Conrad, C. P., & Lithgow-Bertelloni, C. (2009). Modification of the
 345 lithospheric stress field by lateral variations in plate-mantle coupling. *Geophysical*
 346 *Research Letters*, 36(22).
- 347 Nataf, H.-C., & Ricard, Y. (1996). 3SMAC: an a priori tomographic model of the
 348 upper mantle based on geophysical modeling. *Physics of the Earth and Planetary*
 349 *Interiors*, 95(1-2), 101–122.
- 350 O'Neill, C., Lenardic, A., Griffin, W., & O'Reilly, S. (2008). Dynamics of cratons in
 351 an evolving mantle. *Lithos*, 102(1), 12–24.

- 352 Pandey, O. P. (2016). Deep scientific drilling results from Koyna and Killari earth-
 353 quake regions reveal why Indian shield lithosphere is unusual, thin and warm.
 354 *Geoscience frontiers*, 7(5), 851–858.
- 355 Pandey, O. P. (2020). *Geodynamic evolution of the Indian shield: Geophysical as-
 356 pects*. Springer, <https://doi.org/10.1007/978-3-030-40597-7>.
- 357 Paul, J., & Ghosh, A. (2020). Evolution of cratons through the ages: A
 358 time-dependent study. *Earth and Planetary Science Letters*, 531, 115962,
 359 <https://doi.org/10.1016/j.epsl.2019.115962>.
- 360 Paul, J., & Ghosh, A. (2022). Could the Réunion plume have thinned the Indian
 361 craton? *Geology*, 50(3), 346–350.
- 362 Paul, J., Ghosh, A., & Conrad, C. (2019). Traction and strain rate at the base
 363 of the lithosphere: An insight into cratonic stability. *Geophysical Journal Interna-
 364 tional*, 217(2), 1024–1033.
- 365 Pearson, D. (1999). The age of continental roots. *Lithos*, 48(1), 171–194.
- 366 Pearson, D., Carlson, R., Shirey, S., Boyd, F., & Nixon, P. (1995). Stabilisation of
 367 Archaean lithospheric mantle: A Re-Os isotope study of peridotite xenoliths from
 368 the Kaapvaal craton. *Earth and Planetary Science Letters*, 134(3), 341–357.
- 369 Pearson, D., & Wittig, N. (2014). The formation and evolution of cratonic mantle
 370 lithosphere—evidence from mantle xenoliths. In K. Turekian & H. Holland (Eds.),
 371 *In treatise on geochemistry* (p. 255–292). New York: Elsevier.
- 372 Peng, L., Liu, L., & Liu, L. (2022). The fate of delaminated cratonic lithosphere.
 373 *Earth and Planetary Science Letters*, 594, 117740.
- 374 Polet, J., & Anderson, D. (1995). Depth extent of cratons as inferred from tomo-
 375 graphic studies. *Geology*, 23(3), 205–208.
- 376 Ritsema, J., Deuss, a. A., Van Heijst, H., & Woodhouse, J. (2011). S40rts: a degree-
 377 40 shear-velocity model for the mantle from new Rayleigh wave dispersion, tele-
 378 seismic traveltimes and normal-mode splitting function measurements. *Geophysical
 379 Journal International*, 184(3), 1223–1236.
- 380 Rudnick, R., McDonough, W., & O'Connell, R. (1998). Thermal structure, thickness
 381 and composition of continental lithosphere. *Chemical Geology*, 145(3), 395–411.
- 382 Simmons, N. A., Forte, A. M., Boschi, L., & Grand, S. P. (2010). Gypsum: A
 383 joint tomographic model of mantle density and seismic wave speeds. *Journal of
 384 Geophysical Research: Solid Earth*, 115, <https://doi.org/10.1029/2010JB007631>.
- 385 Sleep, N. H. (2003). Survival of Archean cratonal lithosphere. *Journal of Geophysical
 386 Research: Solid Earth*, 108(B6).
- 387 Wang, H., van Hunen, J., Pearson, D. G., & Allen, M. B. (2014). Craton stability
 388 and longevity: The roles of composition-dependent rheology and buoyancy. *Earth
 389 and Planetary Science Letters*, 391, 224–233.
- 390 Wu, F.-Y., Yang, J.-H., Xu, Y.-G., Wilde, S. A., Walker, R. J., et al. (2019). De-
 391 struction of the North China craton in the Mesozoic. *Annual Review of Earth and
 392 Planetary Sciences*, 47(1), 173–195.
- 393 Yoshida, M. (2012). Dynamic role of the rheological contrast between cratonic and
 394 oceanic lithospheres in the longevity of cratonic lithosphere: A three-dimensional
 395 numerical study. *Tectonophysics*, 532, 156–166.
- 396 Yoshida, M., & Yoshizawa, K. (2021). Continental drift with deep cratonic roots.
 397 *Annual Review of Earth and Planetary Sciences*, 49, 117–139.
- 398 Zhong, S. (2001). Role of ocean-continent contrast and continental keels on plate
 399 motion, net rotation of lithosphere, and the geoid. *Journal of Geophysical Re-
 400 search: Solid Earth*, 106(B1), 703–712.
- 401 Zhong, S., Zuber, M., Moresi, L. N., & Gurnis, M. (2000). Role of temperature-
 402 dependent viscosity and surface plates in spherical shell models of mantle convec-
 403 tion. *Journal of Geophysical Research: Solid Earth*, 105(B5), 11063–11082.